JACS Au
AN OPEN ACCESS JOURNAL OF THE AMERICAN CHEMICAL SOCIETY

pubs.acs.org/jacsau
Article

Highly Selective CO_2 Conversion to CH_4 by a N-Doped $HTiNbO_5$/NH_2-UiO-66 Photocatalyst without a Sacrificial Electron Donor

Wenyuan Huang,[#] Ziyi Zhang,[#] Jingwen Xu, Haopeng Cui, Kexin Tang, Danielle Crawshaw, Jinxing Wu, Xiaodong Zhang,* Liang Tang,* and Ning Liu*

Cite This: *JACS Au* 2025, 5, 1184−1195
Read Online
ACCESS | Metrics & More | Article Recommendations | Supporting Information

ABSTRACT: Photocatalytic reduction of CO_2 to value-added chemicals is a promising technology for reducing atmospheric CO_2, but selectively producing a specific product still remains a great challenge. In this study, a Z-scheme heterojunction, N-doped $HTiNbO_5$/NH_2-UiO-66(Zr) (referred to as NH-NU), is developed to integrate the advantages of semiconductor photocatalysts and porous CO_2 adsorbents for CO_2-to-CH_4 conversion. The NH-NU Z-scheme heterojunctions are fabricated via a simple one-pot solvothermal method, enabling the formation of a tight and uniform interface between the two phases, thereby facilitating the separation and transfer of the photoinduced charge carriers, as confirmed by TEM, EPR, electrochemical studies, and work functions. As a result, the as-prepared photocatalyst demonstrates a significant increase in selectivity for CH_4 production through CO_2 photoreduction, achieving a 10-fold enhancement compared to that of the pristine MOF, NH_2-UiO-66. Moreover, there is no obvious decrease in the photocatalytic activity for CH_4 production across four consecutive cycles. In situ FT-IR spectroscopy and DFT calculations reveal that charge-enriched N-doped NH-NU-3 composites stabilize various C_1 intermediates in multistep elementary reactions, leading to superior selectivity in the CO_2-to-CH_4 conversion process. This work establishes that efficient and selective heterogeneous catalytic processes can be achieved through the stabilization of reaction intermediates by designing suitable Z-scheme heterojunctions.

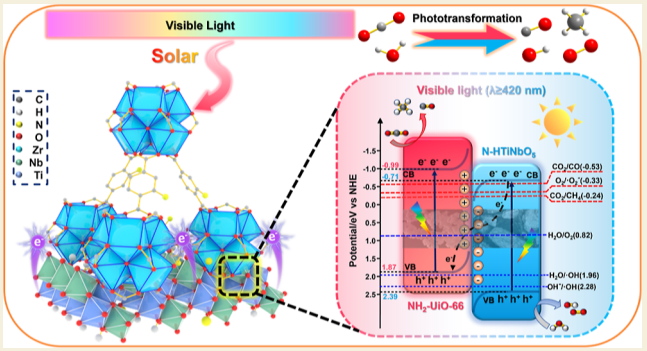

KEYWORDS: *photocatalytic CO_2 reduction, NH_2-UiO-66, N-HTiNbO$_5$, CH_4 production*

1. INTRODUCTION

The conversion of CO_2 into value-added chemicals such as CO, HCOOH, CH_3OH, and CH_4 through catalytic reduction is a promising technology that addresses both the energy crisis and environmental issues we face.[1−3] Photocatalytic conversion of CO_2 has emerged as a sustainable approach for the capture and utilization of CO_2.[4−6] However, CO_2 reduction is a highly energy-intensive process due to the stable C═O bonds in CO_2 (with an extremely high dissociation energy of CO_2 of 805 kJ mol^{-1}).[7] Therefore, the development of efficient and selective photocatalysts proficient in CO_2 adsorption and activation has become a significant interest within the realm of CO_2 photoreduction.

Metal organic frameworks (MOFs) possess an adaptable pore structure, high porosity, and excellent specific surface area.[8,9] MOFs also have a good CO_2 uptake capacity and have been widely applied for CO_2 photoreduction. The Cu and Ni single sites can be successfully incorporated into MOFs to afford MOF-808-CuNi, which shows 99.4% CH_4 selectivity and a production rate of 158.7 μmol g^{-1} h^{-1} with a Ru-based sacrificial reagent.[10] Zr-MBA-Ru/Re-MOF can be prepared via post-synthetic linker exchange (PSE) followed by metalation of MOF-808 and exhibits highly efficient CO_2-to-CO formation with a maximum production rate of 440 μmol g^{-1} h^{-1} in an aqueous medium without any sacrificial electron donor.[11] Adenine-modified MOFs, AD-MOF-2, exhibits a very high HCOOH production rate of 443.2 μmol g^{-1} h^{-1} in pure aqueous solution.[12] However, it is still challenging to produce CH_4 with high selectivity via CO_2 photoreduction using a MOF-based material, especially in an aqueous medium without any sacrificial electron donor. The poor photocatalytic performance of MOF materials may be a result of low electron/hole separation and charge transfer rate. Thus, designing hybrid heterojunctions involving MOFs, capable of adsorbing and activating CO_2, promoting separation and transformation rate of charge carrier to improve reduction efficiency, remains an important yet challenging strategy.

Received: October 22, 2024
Revised: December 9, 2024
Accepted: December 10, 2024
Published: December 19, 2024

https://doi.org/10.1021/jacsau.4c00998
JACS Au 2025, 5, 1184−1195

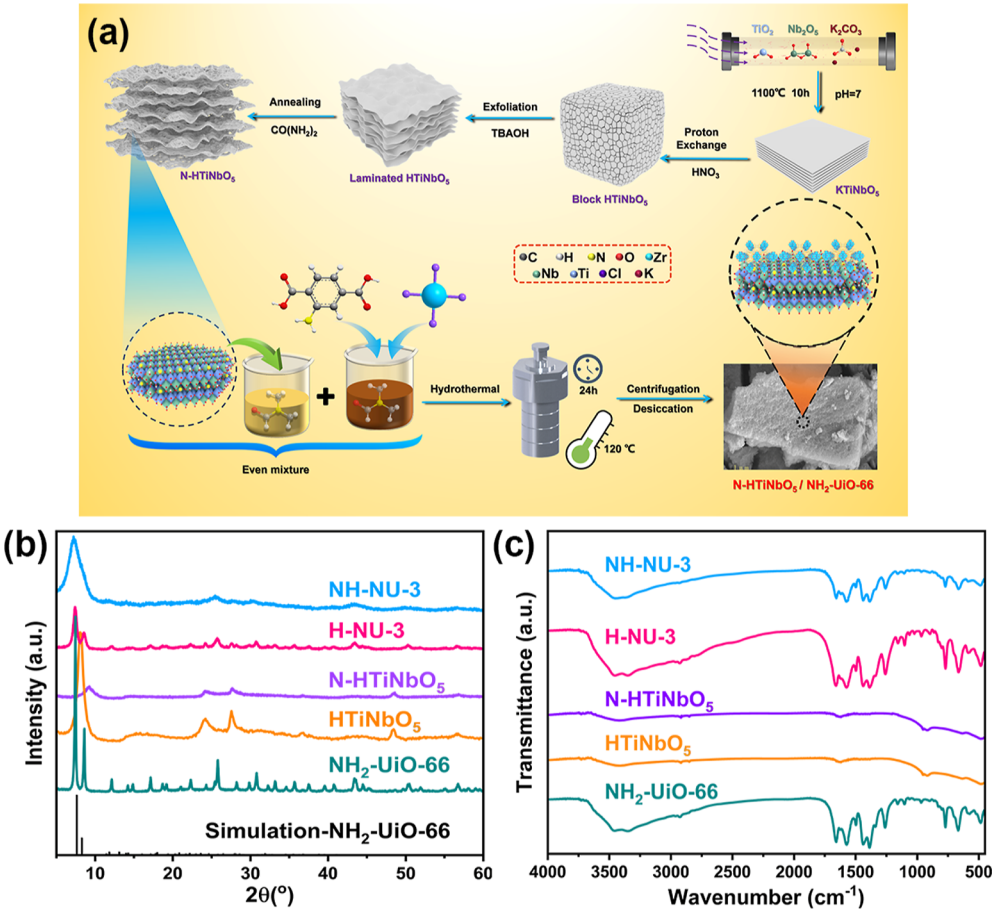

Figure 1. (a) Synthesis processes of NH-NU. (b) X-ray diffraction (XRD) patterns and (c) FT-IR spectra of the as-prepared photocatalysts.

Z-scheme heterojunctions have proven efficient in spatially separating photogenerated electron/hole carriers with high redox capabilities.[13−19] 2D ultrathin Z-scheme $ZnIn_2S_4$/g-C_3N_4 heterojunctions are constructed via in situ growth of $ZnIn_2S_4$ on g-C_3N_4 and exhibit an enhanced photocatalytic hydrogen production rate of 14.8 mmol g^{-1} h^{-1}.[15] The Z-scheme 2D/2D heterojunction of $CsPbBr_3/Bi_2WO_6$ shows an improved CO_2 photoreduction rate of 9.4 μmol g^{-1} h^{-1} for CO and 14.3 μmol g^{-1} h^{-1} for CH_4 with ethyl acetate and isopropyl alcohol as the reaction medium.[16] 100% CO selectivity is obtained from the CO_2 photocatalytic reduction using a lanthanum single atom anchored on a black phosphorus Z-scheme heterojunction.[17] The Z-scheme heterojunction UiO-66/NH_2-MIL-125/g-C_3N_4 is also constructed via a MOF-on-MOF strategy and shows high-performance photocatalytic degradation of ofloxacin antibiotics.[18] However, there are few reports on MOFs-based Z-scheme heterojunctions for selective CO_2 photoreduction to single valuable products, especially in an aqueous medium without any sacrificial electron donor.

Herein, a highly stable MOF NH_2-UiO-66(Zr) has been selected as a platform to develop an advanced MOF-based Z-scheme heterojunction due to its high CO_2 adsorption capability and suitable range of visible light absorption.[20,21] Additionally, $HTiNbO_5$ possesses several characteristics of a layered structure, can be easily synthesized, has favorable charge transfer property, and has been introduced to modify NH_2-UiO-66(Zr) to form a Z-scheme heterojunction to increase the intensity of light absorption and improve the transfer rate of photogenerated charges. The strong adhesion of $HTiNbO_5$ to the MOFs photocatalyst, NH_2-UiO-66, aids the transfer and separation of photocatalytic charge carriers. Furthermore, the introduction of nitrogen into $HTiNbO_5$, to form N-$HTiNbO_5$, can increase the electrical conductivity, whereby the recombination of photogenerated charge carriers is prevented by the Z-scheme heterojunction, allowing the selective formation of the desired product, CH_4, from CO_2 reduction without any sacrificial electron donor.

2. EXPERIMENTAL SECTION

2.1. Materials

In this research, all chemical reagents used were purchased from Sinopharm Chemical Reagent Co. in China. And all chemicals and reagents used in this research were of analytical grade and used without any further purification.

2.2. Preparation of NH_2-UiO-66(Zr)

NH_2-UiO-66(Zr) was synthesized, according to the literature, by a solvothermal method.[21]

2.3. Preparation of $HTiNbO_5$ and N-$HTiNbO_5$

$HTiNbO_5$ nanosheets were prepared as reported with some modifications.[22−26] $KTiNbO_5$ samples were prepared through high-temperature solid-state reactions using TiO_2, Nb_2O_5, and K_2CO_3 with a molar ratio of 2:1:1.1. The well-stirred mixture was reacted in an aluminum crucible in air for 10 h at 1100 °C. The obtained white powder was washed several times with deionized water until the pH value was approximately 7 and then dried at 80 °C to give a white solid.

Proton-exchanged $KTiNbO_5$ ($HTiNbO_5$) was prepared by suspending 1.5 g $KTiNbO_5$ in 150 mL of 6 M HNO_3 solution and stirring for 6 days, whereby the HNO_3 solution was replaced every 2 days. The

https://doi.org/10.1021/jacsau.4c00998
JACS Au 2025, 5, 1184−1195

resulting solid was then washed with H_2O, collected by centrifugation, and dried at room temperature to give a white solid.

The exfoliation of $HTiNbO_5$ was carried out in an aqueous solution of tetrabutylammonium hydroxide (TBAOH). 1 g of $HTiNbO_5$ was added to 100 mL of deionized water, and the pH value was adjusted to 9.5−10 using TBAOH. The mixture was stirred for 7 days, and then the supernatant was obtained following centrifugation. Subsequently, 1 M HCl was added dropwise and a white precipitate formed. The white precipitate was separated and dried using a freeze dryer for 15 h to obtain the layered $HTiNbO_5$ nanosheet.

To synthesize the N-doped $HTiNbO_5$ nanosheet, 1 g of the $HTiNbO_5$ nanosheet and 2 g of urea were mixed and placed in an aluminum crucible, which was then heated to 400 °C for 4 h. The product was washed with 0.1 M HNO_3 and deionized water three times, respectively, before being dried at 70 °C to obtain N-doped $HTiNbO_5$ (N-$HTiNbO_5$).

2.4. Preparation of $HTiNbO_5$/MOF and N-$HTiNbO_5$/MOF

A series of $HTiNbO_5$/MOF and N-$HTiNbO_5$/MOF catalysts were prepared by a solvothermal method, in which the mass of $HTiNbO_5$ or N-$HTiNbO_5$ added was altered. Typically, $HTiNbO_5$ or N-$HTiNbO_5$ solutions were diluted to 50 mL in DMF to give various concentrations and then sonicated overnight. Next, 0.2332 g of $ZrCl_4$ was added to the solution, which was sonicated for 30 min, followed by the addition of 0.1812 g of 2-aminoterephthalic acid and sonication for a further 30 min. Afterward, the mixture was transferred to a Teflon-lined autoclave and crystallized in an oven at 120 °C for 24 h. After cooling to room temperature, the obtained product was centrifuged, repeatedly washed with DMF and methanol, and then dried at 60 °C for 8 h to yield $HTiNbO_5$/NH_2-UiO-66(Zr) (H-NU-X, where X represents the weight content of $HTiNbO_5$) or N-$HTiNbO_5$/NH_2-UiO-66(Zr) (NH-NU-Y, where Y represents the weight content of N-$HTiNbO_5$). Figure 1a illustrates the strategy for the catalyst NH-NU assembly.

2.5. Typical Procedures for Photoactivity Testing

Photocatalytic CO_2 reduction was tested over the as-prepared catalysts H-NU and NH-NU under visible light irradiation. The reaction was carried out in a closed polytetrafluoroethylene reactor with an internal volume of 150 mL. A high-pressure Xe lamp (300 W, 500 mW cm^{-2}) with a cutoff filter ($420 < \lambda < 800$ nm) was used to simulate solar irradiation in the range of visible light. 10 mg of catalyst, 1.6 mL of H_2O, and a stirrer bar were added into the reactor, and CO_2 was continuously introduced into the solution with stirring (500 rpm) for 30 min. Next, the mixture was irradiated with visible light with continuous stirring (500 rpm), and the gas product was quantitatively analyzed by gas chromatography (GC) equipped with an FID detector (with methanizer) at 5 h intervals. The data presented include error bars, which represent the standard deviations across multiple measurements. Each data point was determined at least three times to ensure the accuracy and reproducibility of the results. The error bars reflect the variability observed in the replicate experiments.

2.6. Stability of Photocatalysts

To examine the stability of the photocatalysts, the used catalysts were separated by centrifugation and washed several times with H_2O and methanol and then dried under vacuum at 50 °C overnight. The recovered samples were reused for the next cycle.

2.7. Characterization

The morphology of the as-prepared photocatalysts was measured using a JEM-F200_TFEG transmission electron microscope (TEM) with an accelerating voltage of 200 kV and a GEMINI 300 scanning electronic microscope (SEM). The power XRD patterns were obtained using a Bruker D8 ADVANCE XRD diffractometer operated at 40 kV and 40 mA. The light absorption properties were recorded using a UV-2600 UV−vis diffuse reflectance spectrometer with $BaSO_4$ as the reflectance standard. The N_2 physisorption isotherms were conducted by using a Micromeritics Tristar 3000 analyzer to confirm the Brunauer−Emmett−Teller (BET) surface area and the pore size distributions. The CO_2 adsorption capacity of the materials in this study was determined by a Quantachrome autosorb-iQ-2MP physical adsorption instrument. Before the test, 40−50 mg of the target material was weighed and pretreated at 105 °C for 12 h. The surface properties of the samples were confirmed using Fourier transform infrared spectroscopy (FT-IR, Thermo Scientific Nicolet IS50 Analyzer) and X-ray photoelectron spectra (XPS, A ESCALAB 250Xi system). The reaction intermediates of photocatalytic CO_2 reduction were detected by in situ diffuse reflectance infrared Fourier transform spectroscopy (DRIFTS, Nicolet iS50).

Electrochemical measurements, the photocurrent measurements, and Mott−Schottky (MS) analysis were measured on a CHI600C electrochemical workstation using a three-electrode system, Pt foil as the counter electrode, and a normal hydrogen electrode as the reference electrode. The working electrode was prepared on indium tin oxide glass, and 0.5 M Na_2SO_4 was used as an electrolyte solution.

2.8. Calculation Details

Density functional theory (DFT) calculations were performed using the Vienna Ab Initio Simulation Package (VASP5.4). We used the generalized gradient approximation for the exchange−correlation energy and interatomic interactions with the Perdew−Burke−Ernzerhof adsorption configurations.[27] The cutoff energy was set to 450 eV. Furthermore, (3 × 2 × 1) Monkhorst−Pack *k*-point meshes within the Brillouin zone were used for the structural relaxation calculations.[28,29]

The dimensions of the $HTiNbNO_5$ cell and NH_2-UiO-66 were 6.521 × 3.773 × 16.656 Å ($\alpha = \beta = \gamma = 90°$), $a = b = c = 20.4832$ Å ($\alpha = \beta = \gamma = 90°$). The $HTiNbNO_5$ (0 0 2)- and NH_2-UiO-66 (1 1 1)-exposed surface was chosen for further study.[30,31] A 15 Å vacuum layer was added to prevent lattice interactions. The slabs consisted of a 2 × 2 × 1 supercell with two layers; the top layer was allowed to relax, and the other layer was fixed in its original positions. N doping to $HTiNbNO_5$ was set to bridge between the Nb and Nb position. The conjugate gradient method was used to relax the atomic positions, and the convergence criterion was the presence of a total force of less than 0.05 eV/Å on each ion. The energy convergence criterion for the self-consistent structure cycle was 10^{-5} eV/cell. The magnitude of the work function (Φ) is expressed as the energy required to move an electron from the Fermi energy level to the vacuum energy level and is defined as follows, where $V(\infty)$ is defined as the electrostatic potential of the vacuum layer and E_F denotes the Fermi energy of the surface: $\Phi = V(\infty) - E_F$.

3. RESULTS AND DISCUSSION

3.1. Characterization of the Photocatalysts

The crystallinity of $HTiNbO_5$-, N-$HTiNbO_5$-, NH_2-UiO-66-, and $HTiNbO_5$- or N-$HTiNbO_5$-modified MOF-based photocatalysts was investigated by XRD (Figures 1b and S1−S3). The pattern for $HTiNbO_5$ (Figures 1b and S1) contains peaks at 2θ = 7.9°, 23.9°, and 27.4°, corresponding to crystal planes (002), (011), and (200), respectively, which matches well with reported data.[32,33] Following N doping of $HTiNbO_5$, the peak representing the characteristic reflection (002) shifted to a larger 2θ angle of 9.3° from 7.9°, suggesting that the layered structure is maintained during the heat treatment used during N loading but with a reduced interlayer distance of 9.5 Å, compared to 11.2 Å in the pristine structure (Figures 1b and S1). Moreover, the peaks broaden and reduce in intensity, implying that the N-loading process decreases the crystallinity of the structure.[34] The XRD pattern of NH_2-UiO-66 contains peaks at 2θ = 7.3°, 8.3°, 25.6°, 31.8°, and 43.5° (Figure 1b), consistent with that of the previous reports, therefore confirming the successful preparation of the MOF.[35−37] The doping procedure to synthesize the H-NU series (Figures 1b and S2) did not significantly affect the crystallinity of NH_2-UiO-66; however, the broadening of the peaks in the XRD pattern for the NH-NU-series composites (Figures 1b and S3) suggests that the introduction of N-$HTiNbO_5$ may alter the equilibrium between the organic ligands

https://doi.org/10.1021/jacsau.4c00998
JACS Au 2025, 5, 1184−1195

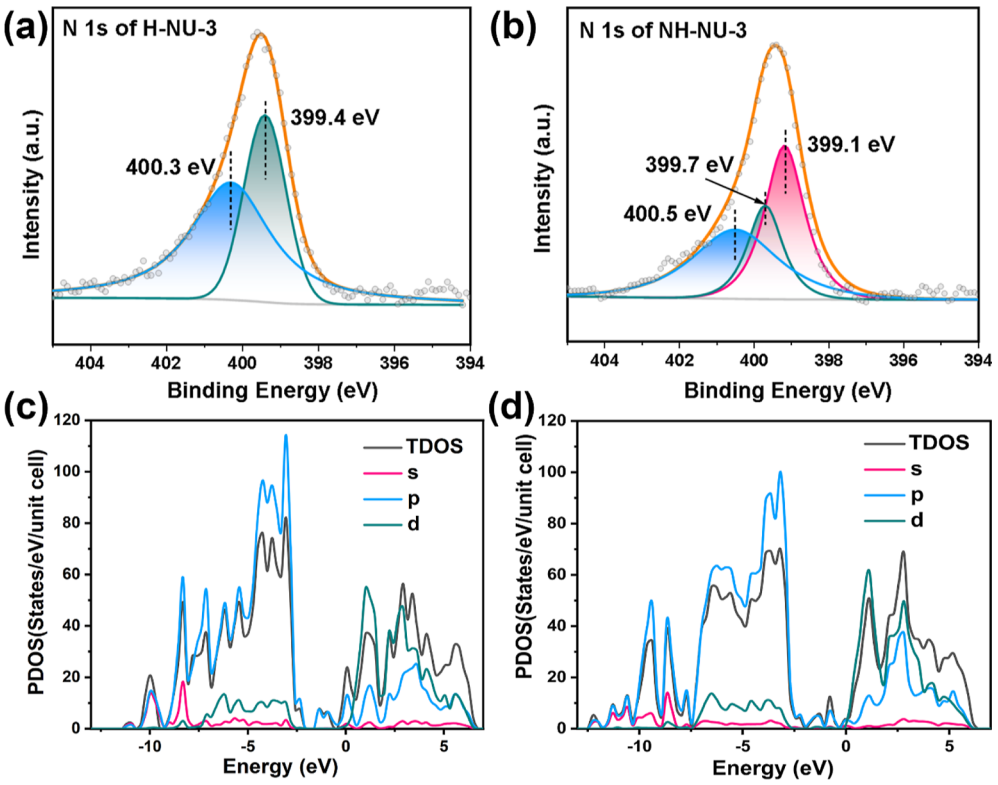

Figure 2. (a,b) N 1s XPS spectra of H-NU-3 (a) and NH-NU-3 (b). (c,d) Total and projected densities of states (TDOS/PDOS) of H-NU-3 (c) and NH-NU-3 (d).

and the metal ions and affect the reactants. As a result, this effect may be employed to control the nucleation and growth processes, leading to a change in the lattice constitution of the MOFs.

Figures 1c and S4 and S5 show the FT-IR spectra of the as-prepared photocatalysts. In the case of NH_2-UiO-66, the peaks at 1255 and 1338 cm^{-1} are attributed to C−N stretching vibrations,[38] and the peaks at 1572 and 3460 cm^{-1} are attributed to the vibration of O−C−O and N−H of organic linkers, respectively.[39] Two new adsorption peaks at 950 and 916 cm^{-1} for the H-NU-series and NH-NU-series composites were observed, which are attributed to Ti−O and Nb−O vibrations in $HTiNbO_5$ or N-$HTiNbO_5$ (Figures S4 and S5),[40] respectively, indicating the successful combination of $HTiNbO_5$ or N-$HTiNbO_5$ nanosheets and the MOF.

The components and chemical state of H-NU-3 and NH-NU-3 were further investigated by XPS (Figures 2a,b and S6−S8). The Ti 2p and Nb 3d spectra demonstrated that $HTiNbO_5$ and N-$HTiNbO_5$ were successfully doped with NH_2-UiO-66 (Figures S6 and S7). The N 1s spectrum of the H-NU-3 sample (Figure 2a) displayed two characteristic peaks at 399.4 and 400.3 eV, respectively, originating from the ligand of NH_2-UiO-66.[36] Additionally, a new peak appeared in NH-NU-3 at approximately 399.1 eV compared to the N 1s peak of H-NU-3,[23] most likely due to the doped nitrogen atoms (Figure 2a,b). According to the literature,[23] the doped nitrogen atoms are likely situated in the interstitial sites of $TiNbO_5^-$ lamellae and chemically bounded to the hydrogen ions incorporated between the $TiNbO_5^-$ layered sheets. Moreover, compared with the peak positions of H-NU-3, the Zr 3d peaks shifted to a lower binding energy and the Ti 2p peaks shifted to a higher binding energy in the XPS patterns of NH-NU-3, indicating that certain electronic interactions have occurred after nitrogen doping (Figure S8).

The total and projected densities of states (TDOS/PDOS) of H-NU and NH-NU hybrids were calculated by DFT as depicted in Figure 2c,d. The introduction of N into $HTiNbO_5$ to construct the NH-NU hybrid shifted the electronic states of the d orbital to the Fermi level compared to that of the H-NU hybrid, which is beneficial for electronic transport, therefore improving the photocatalytic CO_2 reduction activity. Notably, a weak orbital of N was observed close to Fermi level zero, further indicating that N was successfully doped into $HTiNbO_5$.

The SEM and TEM were used to confirm the morphologies and the interfacial structures in H-NU-3 or NH-NU-3 formed from NH_2-UiO-66 and $HTiNbO_5$ or N-doped $HTiNbO_5$ nanosheets.[41] Figure S9 shows octahedron-shaped NH_2-UiO-66 alongside N-$HTiNbO_5$ nanosheets. As illustrated in Figure S10, NH_2-UiO-66 particles were dispersed across the surface of N-$HTiNbO_5$ nanosheets, forming a dense interface contact. HRTEM images were performed to further confirm the intimate interface closely formed between NH_2-UiO-66 and N-$HTiNbO_5$. Fringes with a lattice spacing of approximately 0.33 nm were observed in the HRTEM images, which subsequently indexed to the (200) crystal planes of $HTiNbO_5$. In summary, $HTiNbO_5$ and N-$HTiNbO_5$ were successfully coated with NH_2-UiO-66 in which the close contact facilitates an increased photogenerated charge separation and migration rate, therefore enhancing the efficiency of photocatalytic CO_2 reduction. The N_2 absorption and desorption isotherms of NH_2-UiO-66, H-NU-3, and NH-NU-3 are displayed in Figure S11. The BET surface area over NH_2-UiO-66, H-NU-3, and NH-NU-3 is 746, 574, and 405 $m^2\ g^{-1}$, respectively. The introduction of $HTiNbO_5$ and N-$HTiNbO_5$ decreases the surface area of the composite materials as the loading of $HTiNbO_5$ and N-$HTiNbO_5$ forms heterojunctions, which partially occupy the surface of NH_2-UiO-66. Both H-NU-3 and NH-NU-3 showed

https://doi.org/10.1021/jacsau.4c00998
JACS Au 2025, 5, 1184−1195

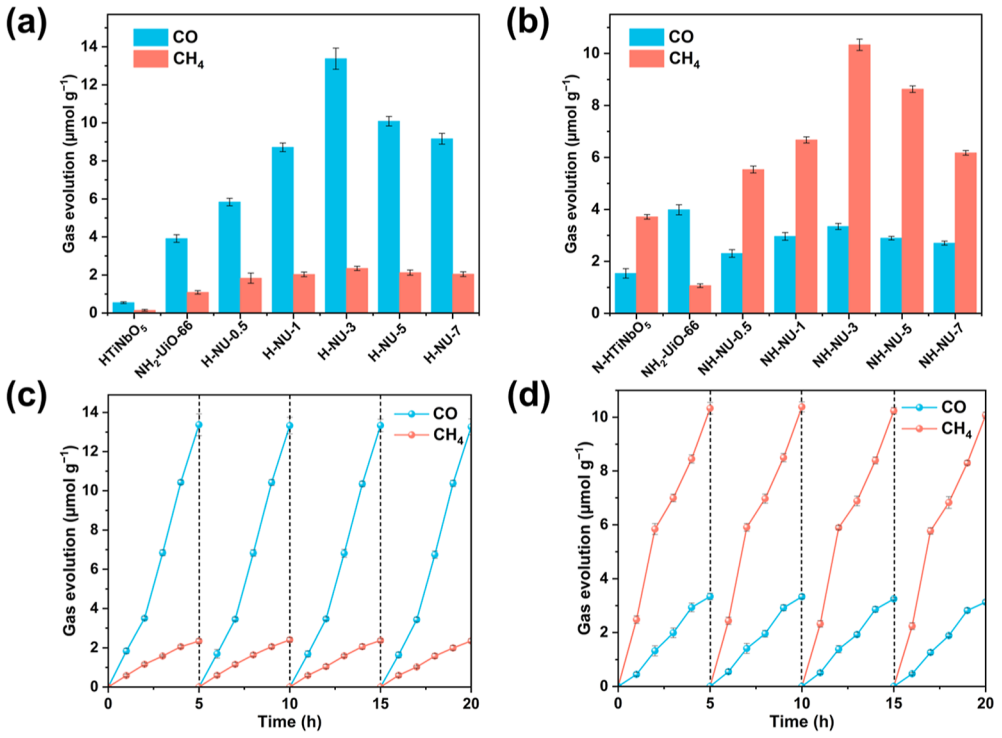

Figure 3. (a,b) Production yield of CO and CH_4 over H-NU-3 (a) and NH-NU-3 (b). (c,d) Cycling measurements for photocatalytic CO_2 reduction to CO and CH_4 over H-NU-3 (c) and NH-NU-3 (d).

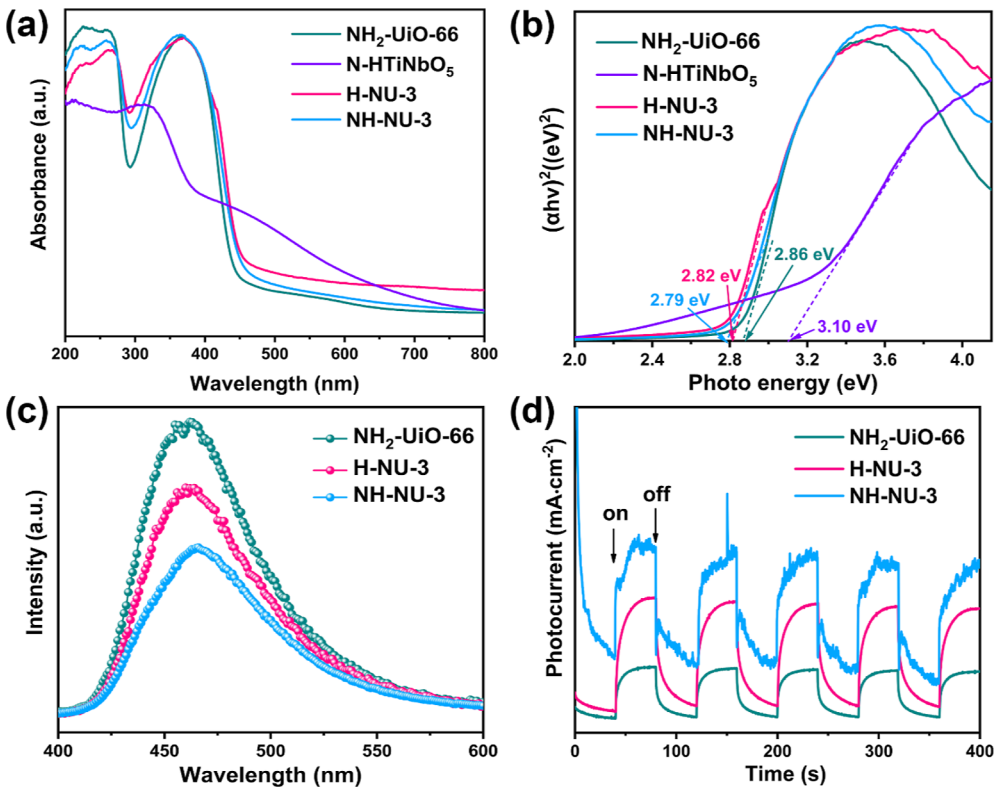

Figure 4. (a,b) UV−vis DRS spectra (a) and the band gaps (b) of NH_2-UiO-66, N-$HTiNbO_5$, H-NU-3, and NH-NU-3. (c,d) PL spectra (c) and transient photocurrent spectra (d) of NH_2-UiO-66, H-NU-3 and NH-NU-3.

promising CO_2 adsorption, as illustrated in Figure S12. This suggests the potential for efficient CO_2 activation and conversion during photocatalytic CO_2 reduction.

3.2. Photocatalytic Performance

The photocatalytic activity of the obtained samples was tested by the CO_2 photoreduction. Control experiments were carried out, in which the reaction was conducted in an N_2 atmosphere,

https://doi.org/10.1021/jacsau.4c00998
JACS Au 2025, 5, 1184−1195

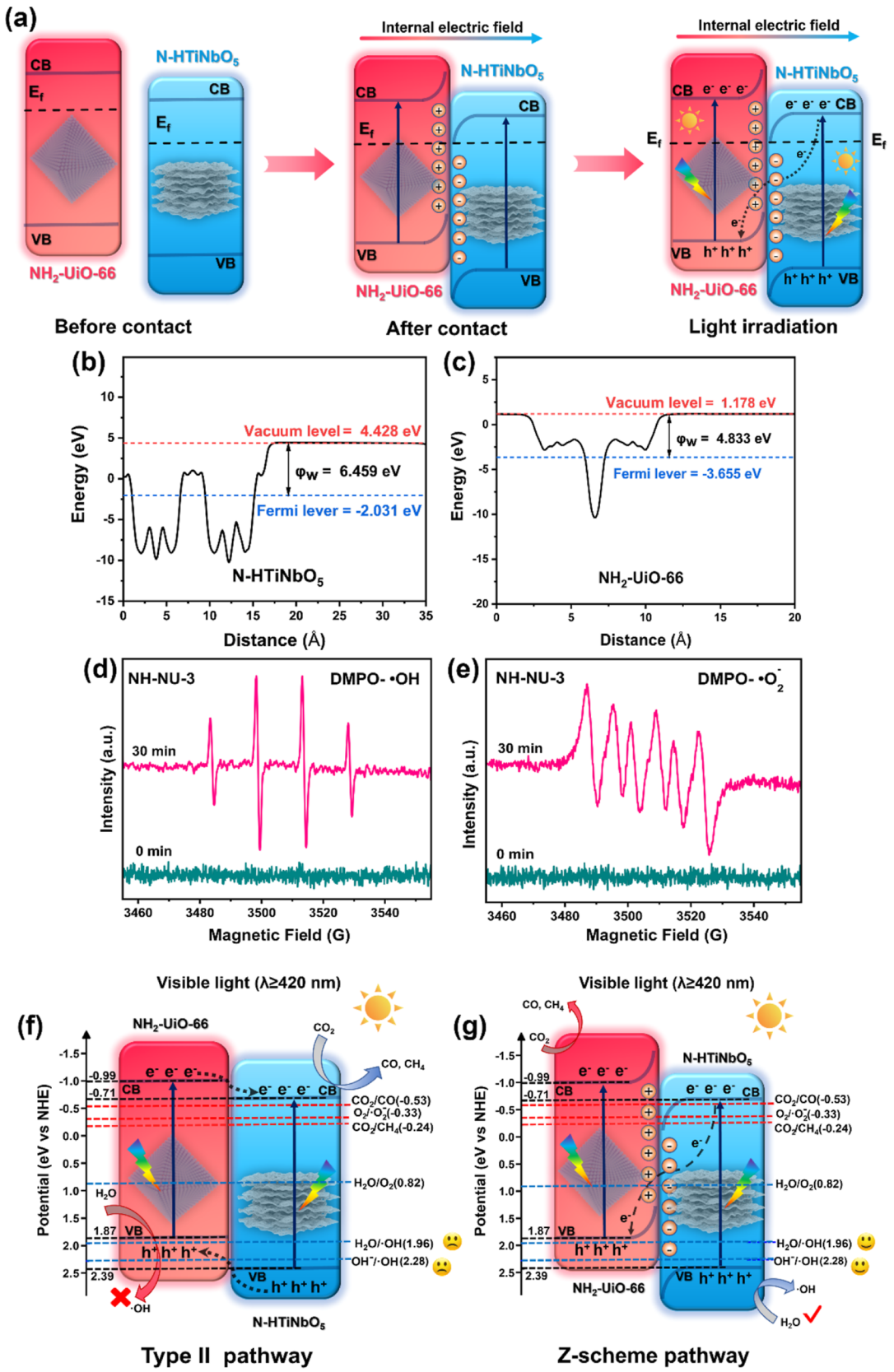

Figure 5. (a) Schematic of directional charge transfer by NH-NU-3 via the Z scheme, calculated work functions of (b) N-HTiNbO$_5$ and (c) NH$_2$-UiO-66, (d) DMPO-$^{\bullet}$OH adducts (in water solution) and (e) DMPO-$^{\bullet}O_2^-$ adducts (in methanol solution) over NH-NU-3 under irradiation for 0 and 30 min, and (f) type II and (g) Z scheme in the NH-NU-3 photocatalyst.

in darkness, without H_2O, or in the absence of catalysts; in each case, no detectable CO/CH_4 products were produced (Figure S13). Thus, within the catalytic system, CO_2 was the only carbon source, confirming that the products, CO and CH_4, were solely

https://doi.org/10.1021/jacsau.4c00998
JACS Au 2025, 5, 1184−1195

derived from the photocatalytic reaction and confirming the need for H_2O and a catalyst exposed to visible light irradiation. As shown in Figure 3a, NH_2-UiO-66 produced approximately 3.9 μmol g^{-1} of CO and 1.1 μmol g^{-1} of CH_4 after 5 h of irradiation. By contrast, the CO and CH_4 production by H-NU-3 was 13.4 μmol g^{-1} and 2.3 μmol g^{-1}, 3.4- and 2.1-fold higher than that of the bare MOF, respectively. Interestingly, NH-NU-3 exhibited an enhanced selectivity for CH_4 evolution of 10.3 μmol g^{-1} over 5 h, nearly 10 times higher than that of pristine NH_2-UiO-66. Moreover, NH-NU-3 shows higher selectivity toward CH_4 formation over CO with a value of 75% (Figure 3b). Without the addition of Ru-based photosensitizers and sacrificial agents, the photocatalytic performance of NH-NU-3 heterojunctions outperforms most similar heterojunctions reported in the literature (Table S1). More importantly, across 4 five h cycles, the gas evolution rate of CO and CH_4 did not significantly change, suggesting that the as-prepared photocatalysts are highly stable under visible light, allowing for reuse in CO_2 reduction (Figure 3c,d). XRD patterns and FT-IR spectra of H-NU-3 and NH-NU-3 were measured and are shown in Figures S14 and S15. These results suggest that the crystal structures and surface functional groups of H-NU-3 and NH-NU-3 are maintained, further demonstrating their excellent photocatalytic stability.

3.3. Photoelectrochemical Test

The light absorption properties of the as-prepared photocatalysts were investigated by ultraviolet−visible diffuse reflectance spectroscopy (UV−vis DRS), as shown in Figures 4a and S16. Pristine NH_2-UiO-66 exhibited strong light absorption in the range of 200−450 nm. The absorption edge of H-NU-3 and NH-NU-3 showed a slight red shift following doping with $HTiNbO_5$ and N-$HTiNbO_5$. Moreover, for the H-NU-3 and NH-NU-3 composites, the visible light absorption intensity increased relative to that of NH_2-UiO-66 between 450 and 800 nm. This increased ability to harvest visible light may enhance the photocatalytic performance of the H-NU-3 and NH-NU-3 composites. The band gap (E_g) of photocatalysts can be calculated by plotting $(\alpha h\nu)^2$ as a function of the photoenergy,[42−44] as displayed in Figure 4b. The band gaps of NH_2-UiO-66(Zr), N-$HTiNbO_5$, H-NU-3, and NH-NU-3 are 2.86, 3.10, 2.82, and 2.79 eV, respectively, indicating that the band gap narrowed upon the introduction of $HTiNbO_5$ and N-doped $HTiNbO_5$. Owing to the improved absorption of visible light, we hypothesize that H-NU-3 and NH-NU-3 can produce more photogenerated carriers, increasing the photocatalytic activity. Moreover, the lifetime of photogenerated hole−electron carriers plays a significant role in the photoreaction process. To evaluate the separation and migration efficiency of photocatalytic carriers, photoluminescence (PL) experiments and transient photocurrent measurements were conducted. The PL spectra of the as-prepared catalysts with an excitation wavelength of 320 nm are shown in Figure 4c. Both H-NU-3 and NH-NU-3 display weaker PL intensity compared to that of NH_2-UiO-66, indicating that photogenerated electron−hole pairs have a longer lifetime within H-NU-3 and NH-NU-3, thus increasing the charge carrier migration rate.[45] Figure 4d shows the photocurrent vs time curves for NH_2-UiO-66, H-NU-3, and NH-NU-3. H-NU-3 and NH-NU-3 display enhanced photocurrent responses compared to that of NH_2-UiO-66, illustrating that the presence of $HTiNbO_5$ and N-$HTiNbO_5$ facilitates the separation of photoinduced electron−hole carriers.

To further study the enhanced photocatalytic activity of CO_2 reduction by H-NU-3 and NH-NU-3, their band structures were determined by Mott−Schottky measurements at a frequency of 1 kHz. As shown in Figures S17−S20, the flat-band potentials of NH_2-UiO-66, N-$HTiNbO_5$, H-NU-3, and NH-NU-3 are −0.89, −0.61, −0.70, and −0.69 eV vs NHE, respectively. Therefore, the conduction-band (CB) potentials of NH_2-UiO-66, N-$HTiNbO_5$, H-NU-3, and NH-NU-3 are −0.99, −0.71, −0.80, and −0.79 eV vs NHE, respectively.[46,47] Based on the formula of $E_{CB} = E_{VB} - E_g$, the valence bands (VB) of NH_2-UiO-66, N-$HTiNbO_5$, H-NU-3, and NH-NU-3 are 1.87, 2.39, 2.02, and 2.00 eV vs NHE, respectively.

3.4. Mechanism Study

The band structures of N-$HTiNbO_5$ and NH_2-UiO-66 before and after the formation of the heterojunction are displayed in Figure 5a. Upon heterojunction formation and irradiation with visible light, the photogenerated electrons in the CB of N-$HTiNbO_5$ were efficiently transferred to the VB of NH_2-UiO-66 via the Z-scheme pathway. The increased lifetime of the photogenerated electron−hole pairs within the NH-NU-3 heterojunctions produces more active sites and increases the activity of photocatalytic CO_2 reduction. To further investigate the charge transfer mechanism of the Z scheme in NH-NU-3, it is crucial to determine the work function of N-$HTiNbO_5$ and NH_2-UiO-66, respectively.[36,48] DFT calculations were applied to investigate the interfacial charge transfer pathways, as shown in Figure 5b,c. The work functions (Φ) of N-$HTiNbO_5$ and NH_2-UiO-66 were calculated to be 6.459 and 4.833 eV, respectively, and the Fermi level of N-$HTiNbO_5$ and NH_2-UiO-66 was calculated to be −2.031 eV and −3.655 eV, respectively, based on the electrostatic potentials between the vacuum level (E_{vac}) and the Fermi level (E_F). Since the work function of N-$HTiNbO_5$ is larger than that of NH_2-UiO-66 and the Fermi level position of N-$HTiNbO_5$ is lower than that of NH_2-UiO-66, the electrons can be easily transferred from NH_2-UiO-66 to N-$HTiNbO_5$ to form an endogenous electric field in the absence of light. Furthermore, the electron paramagnetic resonance (EPR) spectra of the active $^{\bullet}OH$ and $^{\bullet}O_2^-$ radicals further confirm that the Z-scheme mechanism occurs within the NH-NU-3 heterojunctions, as shown in Figure 5d,e. Most significantly, when NH-NU-3 was irradiated with visible light, DMPO-$^{\bullet}OH$ and DMPO-$^{\bullet}O_2^-$ signals were observed, suggesting that the oxidation potential of the photoexcited holes within the VB of either NH_2-UiO-66 or N-$HTiNbO_5$ is higher than the redox potentials of both the $OH^-/^{\bullet}OH$ (2.28 eV vs NHE), H_2O/O_2 (0.82 eV vs NHE), and $H_2O/^{\bullet}OH$ (1.96 eV vs NHE) couples.[12,49] As EPR is unable to distinguish between the oxidation potentials of the 2 VBs, UV−vis DRS and Mott−Schottky analyses were used to confirm that the VB of N-$HTiNbO_5$ is higher than that of NH_2-UiO-66. Moreover, the reduction potential of the photoexcited electrons in the CB of both NH_2-UiO-66 and N-$HTiNbO_5$ was less than the redox potential of CO_2/CH_4 (-0.24 eV vs NHE), CO_2/CO (−0.53 eV vs NHE), and $O_2/^{\bullet}O_2^-$(−0.33 eV vs NHE), indicating the NH-NU-3 heterojunction has the ability to reduce CO_2 in water (Figure 5f,e).[50−52]

Of the two possible mechanisms, the type-II heterojunction mechanism (Figure 5f) involves the migration of electrons from the CB of NH_2-UiO-66 to the CB of N-$HTiNbO_5$ and moreover for the holes to be transferred from the VB of N-$HTiNbO_5$ to the VB of NH_2-UiO-66. However, the potential of the VB in NH_2-UiO-66 is too low to facilitate the oxidation of H_2O to generate

https://doi.org/10.1021/jacsau.4c00998
JACS Au 2025, 5, 1184−1195

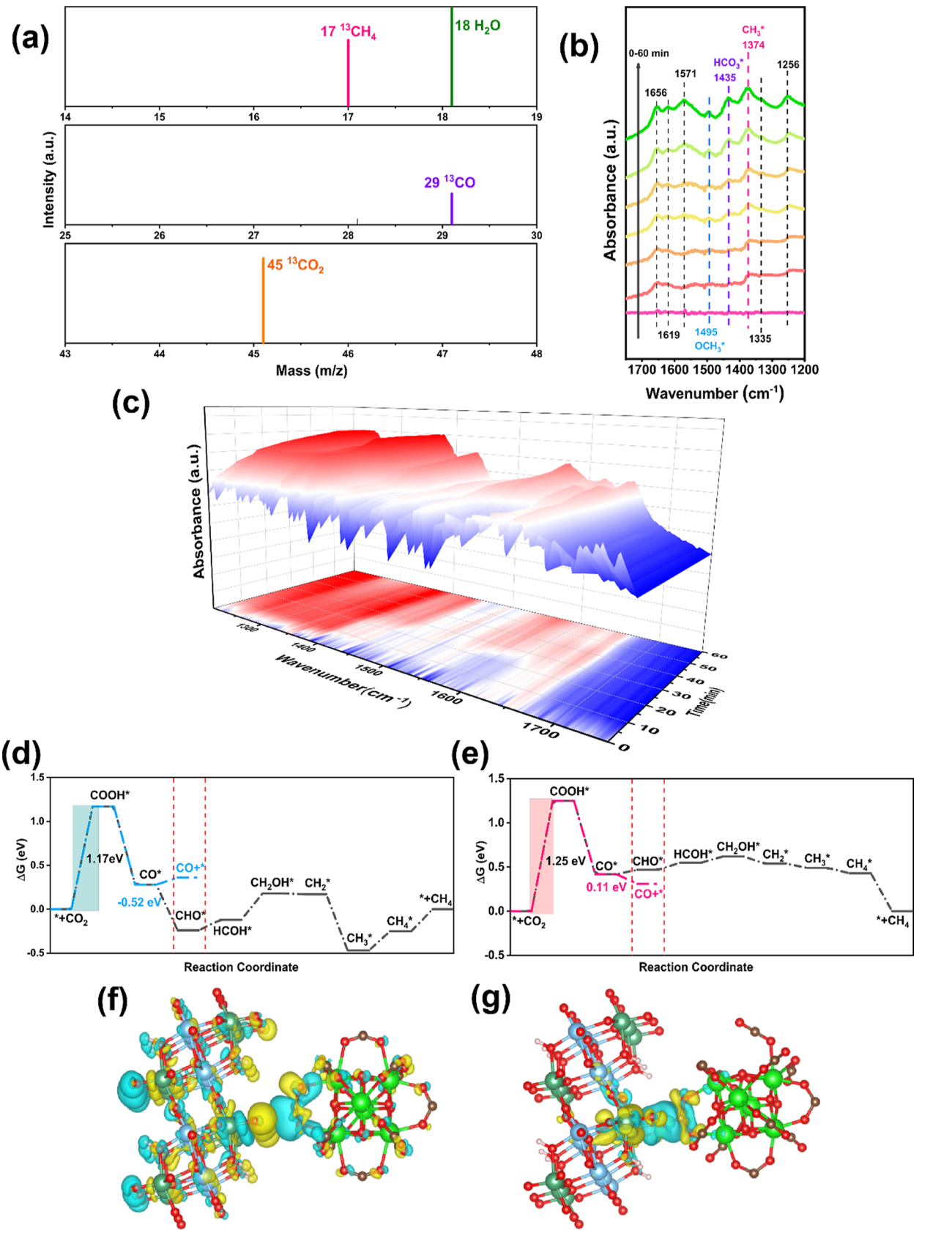

Figure 6. (a) Mass spectra of CH_4 and CO which obtained from the photoreduction of $^{13}CO_2$ over NH-NU-3. (b) In situ DRIFTS spectra at 1200−1750 cm^{-1} taken during the CO_2 photoreduction process to detect the reaction intermediates within NH-NU-3. (c) Three-dimensional in situ FT-IR spectra of the photocatalytic CO_2 reduction reaction. (d,e) Gibbs free energy diagrams of CO_2 photoreduction to CH_4 over NH-NU-3 (d) and H-NU-3 (e). (f,g) Cross-sectional view of charge density difference of NH-NU-3 (f) and H-NU-3 (g).

https://doi.org/10.1021/jacsau.4c00998
JACS Au 2025, 5, 1184−1195

•OH, which is detected by EPR. Therefore, the Z-scheme mechanism justifies the transfer of photoexcited charge carriers rather than the type-II heterojunction mechanism (Figure 5g). Additionally, the analysis of charge densities of states (TDOS/PDOS) (Figure 2c,d) and charge density difference of H-NU-3 and NH-NU-3 (Figure 6f,g) indicate that the charge density on the interface between $HTiNbO_5$ and NH_2-UiO-66 increases after N-doped modification, boosting the electron transferring and further improving the CO_2 photoreduction rate without a sacrificial electron donor.

$^{13}CO_2$ and $H_2{}^{18}O$ labeling experiments were conducted to confirm the derivation of the products, respectively. The signals of $^{13}CH_4$ (m/z = 17), ^{13}CO (m/z = 29), and $^{18}O_2$ (m/z = 36) confirmed that the detected products were the results of photocatalytic CO_2 and H_2O reduction over NH-NU-3 (Figures 6a and S21). In situ DRIFTS was used to identify the reaction intermediates in the process of photocatalytic CO_2 reduction over NH-NU-3 (Figure 6b,c). The peaks at 1656, 1335, and 1256 cm^{-1} are attributed to the C═O stretch, the C−O stretch, and the O−H deformation of *COOH, respectively, which are recognized as crucial intermediates in the process of CO_2 reduction to CO.[53,54] The absorption bands at 1374 and 1495 cm^{-1} are assigned to the $*CH_3$ and $*OCH_3$ groups, respectively, the vital intermediates for the production of CH_4 from CO_2 photoreduction.[7,10,55−59]

To further explore the possible reaction pathway of CO_2 photoreduction over NH-NU-3, DFT calculations were performed to uncover the role of N-$HTiNbO_5$ in achieving the high selectivity toward CH_4.[60] As displayed in Figure 6d,e, the formation of *COOH is the rate-limiting step (in CO_2 reduction) for NH_2-UiO-66, H-NU-3, and NH-NU-3, in which the NH-NU-3 catalyst exhibited the lowest *COOH formation energy. This may be attributed to the increased charge density at the interface between $HTiNbO_5$ and NH_2-UiO-66 upon the introduction of N (Figure 6f,g). Therefore, the charge-enriched interface can more efficiently stabilize the rate-limiting *COOH intermediates. Moreover, in the case of NH-NU-3, the Gibbs free energy of CHO* was smaller than the desorption energy of CO+*, meaning that the formation of CHO* is a spontaneous exothermic process. On the other hand, CO* desorption is endothermic with a large activation energy barrier, as shown in Figure 6d. Thus, it is more thermodynamically favorable for NH-NU-3 to produce CHO* via the protonation of CO* rather than by generating CO molecules from the desorption of CO*. This accounts for the high CH_4 selectivity from the CO_2 photoreduction. In contrast, for H-NU-3, both hydrogenation and desorption of the CO* group are endothermic with a high potential barrier (Figure 6e). As $\Delta G(CO^{+}*)$ is lower than $\Delta G(CHO*)$, CO formation at the surface of H-NU-3 is favored but may also occur by protonation of the CO* group.

4. CONCLUSIONS

In summary, highly efficient visible light Z-scheme heterojunction photocatalysts based on NH_2-UiO-66 and H-$TiNbO_5$ (with and without nitrogen doping) have been developed via a facile one-pot solvothermal process. Both H-NU-3 and NH-NU-3 show significantly higher CO_2 photoreduction activity than that of the pristine MOF, NH_2-UiO-66. Interestingly, N-doped $HTiNbO_5$-modified MOFs show high selectivity in the formation of CH_4, whereas $HTiNbO_5$-modified MOFs display increased selectivity for CO production without any sacrificial electron donor. In situ DRIFTS spectra and Gibbs free energy calculations elucidated that these additional N sites can form charge-enriched interfaces, which lower the overall activation energy barrier. Moreover, the charge-enriched interfaces alter the protonation reaction pathway energy from endoergic to exoergic, thus altering the reaction pathway to produce CH4 rather than CO. Therefore, NH-NU-3 catalyze the highly selective photoreduction of CO_2 toward CH_4, nearly 10 times higher than that of NH_2-UiO-66. This work demonstrates that the selectivity and efficiency of CO_2 reduction can be effectively controlled by the introduction of heteroatom-modified Z-scheme materials.

■ ASSOCIATED CONTENT

Supporting Information

The Supporting Information is available free of charge at https://pubs.acs.org/doi/10.1021/jacsau.4c00998.

XRD and FT-IR patterns of all catalysts; XPS spectra of H-NU-3 and NH-NU-3; SEM and HRTEM images; N_2 and CO_2 adsorption−desorption isotherms; control experiments; UV−vis DRS spectra of all catalysts; Mott−Schottky plots; and $^{18}O_2$ mass spectrum and comparison of photocatalytic properties with this work (PDF)

■ AUTHOR INFORMATION

Corresponding Authors

Xiaodong Zhang − *School of Environment and Architecture, University of Shanghai for Science and Technology, Shanghai 200093, China; Shanghai Noncarbon Energy Conversion and Utilization Institute, Shanghai 200240, P. R. China;* orcid.org/0000-0003-2217-6173; Email: fatzhxd@126.com

Liang Tang − *Key Laboratory of Organic Compound Pollution Control Engineering (MOE), School of Environmental and Chemical Engineering, Shanghai University, Shanghai 200444, P. R. China;* orcid.org/0000-0001-9079-2942; Email: tang1liang@shu.edu.cn

Ning Liu − *School of Environment and Architecture, University of Shanghai for Science and Technology, Shanghai 200093, China; Shanghai Noncarbon Energy Conversion and Utilization Institute, Shanghai 200240, P. R. China;* orcid.org/0000-0001-7600-4233; Email: liuning6910@163.com

Authors

Wenyuan Huang − *School of Environment and Architecture, University of Shanghai for Science and Technology, Shanghai 200093, China; College of Chemistry and Molecular Engineering, Beijing National Laboratory for Molecular Sciences, Peking University, Beijing 100871, China*

Ziyi Zhang − *School of Environment and Architecture, University of Shanghai for Science and Technology, Shanghai 200093, China*

Jingwen Xu − *School of Environment and Architecture, University of Shanghai for Science and Technology, Shanghai 200093, China*

Haopeng Cui − *School of Environment and Architecture, University of Shanghai for Science and Technology, Shanghai 200093, China*

Kexin Tang − *School of Environment and Architecture, University of Shanghai for Science and Technology, Shanghai 200093, China*

Danielle Crawshaw − *Department of Chemistry, The University of Manchester, Manchester M13 9PL, U.K.*
Jinxing Wu − *School of Environment and Architecture, University of Shanghai for Science and Technology, Shanghai 200093, China*

Complete contact information is available at: https://pubs.acs.org/10.1021/jacsau.4c00998

Author Contributions

#W.H. and Z.Z. contributed equally. The manuscript was written through contributions of all authors. All authors have given approval to the final version of the manuscript. CRediT: **Wenyuan Huang** writing - original draft; **Ziyi Zhang** writing - original draft; **Jingwen Xu** data curation; **Haopeng Cui** software; **Kexin Tang** formal analysis; **Danielle Crawshaw** resources; **Jinxing Wu** data curation; **Xiaodong Zhang** writing - review & editing; **Liang Tang** writing - review & editing; **Ning Liu** funding acquisition, writing - review & editing.

Notes

The authors declare no competing financial interest.

■ ACKNOWLEDGMENTS

The authors thank the National Natural Science Foundation of China (Nos. 12075147, 42177405, and 12075152) and Shanghai Pujiang Program (2020PJD036) for the financial support. The authors also thank Ella Clark from KU Leuven for her assistance with proofreading.

■ REFERENCES

(1) Chu, S.; Majumdar, A. Opportunities and Challenges for A Sustainable Energy Future. *Nature* **2012**, *488* (7411), 294−303.
(2) Yang, D.; Wang, J.; Wang, Q.; Yuan, Z.; Dai, Y.; Zhou, C.; Wan, X.; Zhang, Q.; Yang, Y. Electrocatalytic CO_2 Reduction over Atomically Precise Metal Nanoclusters Protected by Organic Ligands. *ACS Nano* **2022**, *16* (10), 15681−15704.
(3) Qi, G.; Ba, D.; Zhang, Y.; Jiang, X.; Chen, Z.; Yang, M.; Cao, J.; Dong, W.; Zhao, J.; Li, D.; Zhang, Q. Constructing an Asymmetric Covalent Triazine Framework to Boost the Efficiency and Selectivity of Visible-Light-Driven CO_2 Photoreduction. *Adv. Sci.* **2024**, *11* (28), 2402645.
(4) Huang, P. P.; Huang, J. H.; Pantovich, S. A.; Carl, A. D.; Fenton, T. G.; Caputo, C. A.; Grimm, R. L.; Frenkel, A. I.; Li, G. H. Selective CO_2 Reduction Catalyzed by Single Cobalt Sites on Carbon Nitride under Visible-Light Irradiation. *J. Am. Chem. Soc.* **2018**, *140* (47), 16042−16047.
(5) Tang, M.; Tang, K.; Wang, D.; Yu, J.; Kong, W.; Shao, H.; Li, F.; Zhang, X.; Lei, J.; Liu, N. Photocatalytic Reduction of CO_2 in Aqueous Phase Using Amino-Functionalized MOFs Loaded with Hydroxy-Functionalized Graphene Quantum Dots. *Sep. Purif. Technol.* **2024**, *329*, 125245.
(6) Liu, W. B.; Li, X. K.; Wang, C. M.; Pan, H. H.; Liu, W. P.; Wang, K.; Zeng, Q. D.; Wang, R. M.; Jiang, J. Z. A Scalable General Synthetic Approach toward Ultrathin Imine-Linked Two-Dimensional Covalent Organic Framework Nanosheets for Photocatalytic CO_2 Reduction. *J. Am. Chem. Soc.* **2019**, *141* (43), 17431−17440.
(7) Tang, K.; Zhang, Z.; Zhou, D.; Xu, J.; Cui, H.; Li, F.; Zhang, X.; Lei, J.; Tang, L.; Liu, N. Bimetallic Materials as Catalysts for Photocatalytic CO_2 Reduction to Value-Added Chemicals: A Review. *Sep. Purif. Technol.* **2025**, *356*, 129952.
(8) Xu, D.; Dong, W.; Li, M.; Han, H.; Zhao, J.; Li, D.; Zhang, Q. Encapsulating Organic Dyes in Metal-Organic Frameworks for Color-Tunable and High-Efficiency White-Light-Emitting Properties. *Inorg. Chem.* **2022**, *61* (51), 21107−21114.
(9) Yuan, K.; Gong, B.; Peng, C.; Feng, Y.; Hu, Y.; Chen, K.; Chen, D.; Hao, D. Porphyrin Modified UiO-66-NH_2 for Highly Efficient Photoreduction of Cr(VI) under Visible Light. *Catalysts* **2023**, *13* (7), 1073.
(10) Li, J.; Huang, H.; Xue, W.; Sun, K.; Song, X.; Wu, C.; Nie, L.; Li, Y.; Liu, C.; Pan, Y.; Jiang, H.; Mei, D.; Zhong, C. Self-Adaptive Dual-Metal-Site Pairs in Metal-Organic Frameworks for Selective CO_2 Photoreduction to CH_4. *Nat. Catal.* **2021**, *4* (8), 719−729.
(11) Karmakar, S.; Barman, S.; Rahimi, F. A.; Maji, T. K. Covalent Grafting of Molecular Photosensitizer and Catalyst on MOF-808: Effect of Pore Confinement Toward Visible Light-driven CO_2 Reduction in Water. *Energy Environ. Sci.* **2021**, *14* (4), 2429−2440.
(12) Li, N.; Liu, J.; Liu, J.; Dong, L.; Xin, Z.; Teng, Y.; Lan, Y.-Q. Adenine Components in Biomimetic Metal-Organic Frameworks for Efficient CO_2 Photoconversion. *Angew. Chem., Int. Ed.* **2019**, *58* (16), 5226−5231.
(13) Wang, Q.; Zheng, S.; Ma, W.; Qian, J.; Huang, L.; Deng, H.; Zhou, Q.; Zheng, S.; Li, S.; Du, H.; Li, Q.; Hao, D.; Yang, G. Facile Synthesis of Direct Z-scheme PPy/NH_2-UiO-66 Heterojunction for Enhanced Photocatalytic Cr(VI) Reduction, Industrial Electroplating Wastewater Treatment, and TetracyclineDegradation. *Appl. Catal., B* **2024**, *344*, 123669.
(14) Zheng, S.; Du, H.; Yang, L.; Tan, M.; Li, N.; Fu, Y.; Hao, D.; Wang, Q. PDINH Bridged NH_2-UiO-66(Zr) Z-scheme Heterojunction for Promoted Photocatalytic Cr(VI) Reduction and Antibacterial activity. *J. Hazard. Mater.* **2023**, *447*, 130849.
(15) Tan, M.; Ma, Y.; Yu, C.; Luan, Q.; Li, J.; Liu, C.; Dong, W.; Su, Y.; Qiao, L.; Gao, L.; Lu, Q.; Bai, Y. Boosting Photocatalytic Hydrogen Production *via* Interfacial Engineering on 2D Ultrathin Z-Scheme $ZnIn_2S_4$/g-C_3N_4 Heterojunction. *Adv. Funct. Mater.* **2022**, *32* (14), 2111740.
(16) Jiang, Y.; Chen, H.; Li, J.; Liao, J.; Zhang, H.; Wang, X.; Kuang, D. Z-Scheme 2D/2D Heterojunction of $CsPbBr_3$/Bi_2WO_6 for Improved Photocatalytic CO_2 Reduction. *Adv. Funct. Mater.* **2020**, *30* (50), 2004293.
(17) Wang, Q.; Dong, L.; Li, M.; Lu, H.; Wei, G.; Qu, Y.; Wang, G. Z-scheme Heterojunction Photocatalyst Based on Lanthanum Single-Atom Anchored on Black Phosphorus for Regulating Surface Active Sites, therefore Enhancing Photocatalytic CO_2 Reduction with≈100% CO Selectivity. *Adv. Funct. Mater.* **2022**, *32* (41), 2207330.
(18) Sepehrmansourie, H.; Alamgholiloo, H.; Noroozi Pesyan, N.; Zolfigol, M. A. A MOF-on-MOF Strategy to Construct Double Z-scheme Heterojunction for High-Performance Photocatalytic Degradation. *Appl. Catal., B* **2023**, *321*, 122082.
(19) Yang, M.; Cao, J.; Qi, G.; Shen, X.; Yan, G.; Wang, Y.; Dong, W.; Zhao, J.; Li, D.; Zhang, Q. Construction of Low-Cost Z-Scheme Heterojunction Cu_2O/PCN-250 Photocatalysts Simultaneously for the Enhanced Photoreduction of CO_2 to Alcohols and Photooxidation of Water. *Inorg. Chem.* **2023**, *62* (39), 15963−15970.
(20) Crake, A.; Christoforidis, K. C.; Kafizas, A.; Zafeiratos, S.; Petit, C. CO_2 Capture and Photocatalytic Reduction Using Bifunctional TiO_2/MOF Nanocomposites under UV−vis Irradiation. *Appl. Catal., B* **2017**, *210*, 131−140.
(21) Bi, F.; Wei, J.; Gao, B.; Ma, S.; Liu, N.; Xu, J.; Liu, B.; Huang, Y.; Zhang, X. How the Most Neglected Residual Species in MOF-Based Catalysts Involved in Catalytic Reactions to Form Toxic Byproducts. *Environ. Sci. Technol.* **2024**, *58* (44), 19797−19806.
(22) Lin, H.-Y.; Chang, Y.-S. Photocatalytic Water Splitting on Au/$HTiNbO_5$ Nanosheets. *Int. J. Hydrogen Energy* **2014**, *39* (7), 3118−3126.
(23) Zhai, Z.; Huang, Y.; Xu, L.; Yang, X.; Hu, C.; Zhang, L.; Fan, Y.; Hou, W. Thermostable Nitrogen-Doped $HTiNbO_5$ Nanosheets with A High Visible-Light Photocatalytic Activity. *Nano Res.* **2011**, *4* (7), 635−647.
(24) Liu, N.; Hu, B.; Tang, K.; Xia, T.; Li, F.; Quan, G.; Zhang, X.; Tang, L. Assembling UiO-66 into Layered $HTiNbO_5$ Nanosheets for Efficient Photocatalytic CO_2 Reduction. *Surf. Interfaces.* **2023**, *41*, 103134.
(25) Zhai, Z.; Hu, C.; Yang, X.; Zhang, L.; Liu, C.; Fan, Y.; Hou, W. Nitrogen-Doped Mesoporous Nanohybrids of TiO_2 Nanoparticles and $HTiNbO_5$ Nanosheets with A High Visible-Light Photocatalytic

Activity and A Good Biocompatibility. *J. Mater. Chem.* **2012**, *22* (36), 19122−19131.
(26) Lv, W.; He, J.; Xu, A.; Hu, L.; Da, L. Structure and Photocatalytic Activity of Nitrogen-doped $HTiNbO_5$ Nanosheet Aggregation. *Nano* **2017**, *12* (01), 1750003.
(27) Kresse, G.; Furthmüller, J. Efficient Iterative Schemes for Ab Initio Total-Energy Calculations Using A Plane-Wave Basis Set. *Phys. Rev. B* **1996**, *54* (16), 11169−11186.
(28) Han, L.; Jing, F.; zhang, J.; Luo, X.; Zhong, Y.; Wang, K.; Zang, S.; Teng, D.; Liu, Y.; Chen, J.; et al. Environment Friendly and Remarkably Efficient Photocatalytic Hydrogen Evolution Based on Metal Organic Framework Derived Hexagonal/Cubic In_2O_3 Phase-Junction. *Appl. Catal., B* **2021**, *282*, 119602.
(29) Setyawan, W.; Curtarolo, S. High-Throughput Electronic Band Structure Calculations: Challenges and Tools. *Comput. Mater. Sci.* **2010**, *49* (2), 299−312.
(30) Zhai, Z.; Yang, X.; Xu, L.; Hu, C.; Zhang, L.; Hou, W.; Fan, Y. Novel Mesoporous NiO/$HTiNbO_5$ Nanohybrids with High Visible-Light Photocatalytic Activity and Good Biocompatibility. *Nanoscale* **2012**, *4* (2), 547−556.
(31) Zhao, C.; Zhang, Y.; Jiang, H.; Chen, J.; Liu, Y.; Liang, Q.; Zhou, M.; Li, Z.; Zhou, Y. Combined Effects of Octahedron NH_2-UiO-66 and Flowerlike $ZnIn_2S_4$ Microspheres for Photocatalytic Dye Degradation and Hydrogen Evolution under Visible Light. *J. Phys. Chem. C* **2019**, *123* (29), 18037−18049.
(32) He, J.; Li, Q. J.; Tang, Y.; Yang, P.; Li, A.; Li, R.; Li, H. Z. Characterization of $HNbMoO_6$, $HNbWO_6$ and $HTiNbO_5$ as Solid Acids and Their Catalytic Properties for Esterification Reaction. *Appl. Catal., A* **2012**, *443*−*444*, 145−152.
(33) Zhang, L.; Hu, C.; Cheng, L.; Ding, W.; Hou, W.; Chen, J. S-doped $HTiNbO_5$ Nanosheets: A Novel Efficient Visible-Light Photocatalyst. *Chin. J. Catal.* **2013**, *34* (11), 2089−2097.
(34) Wang, S.; Zhang, X.; Dao, X.; Cheng, X.; Sun, W. Cu_2O@Cu@UiO-66-NH_2 Ternary Nanocubes for Photocatalytic CO_2 Reduction. *ACS Appl. Nano Mater.* **2020**, *3* (10), 10437−10445.
(35) Zhang, Z.; Wang, S.; Bao, M.; Ren, J.; Pei, S.; Yu, S.; Ke, J. Construction of Ternary Ag/AgCl/NH_2-UiO-66 Hybridized Heterojunction for Effective Photocatalytic Hexavalent Chromium Reduction. *J. Colloid Interface Sci.* **2019**, *555*, 342−351.
(36) Sun, J.; Guan, Y.; Yang, G.; Qiu, S.; Shao, H.; Wang, Y.; Li, G.; Xiao, S. S-Scheme Photocatalyst NH_2-UiO-66/CuZnS with Enhanced Photothermal-Assisted CO_2 Reduction Performances. *ACS Sustainable Chem. Eng.* **2023**, *11* (40), 14827−14840.
(37) Lu, Z.; Guo, L.; Bi, F.; Ma, S.; Shen, Q.; Qiao, R.; Zhang, X. Insight into the Degradation Mechanism of Mixed VOCs Oxidation over Pd/UiO-66(Ce) Catalysts: Combination of Operando Spectroscopy and Theoretical Calculation. *Sep. Purif. Technol.* **2025**, *354*, 129443.
(38) Kandiah, M.; Usseglio, S.; Svelle, S.; Olsbye, U.; Lillerud, K. P.; Tilset, M. Post-Synthetic Modification of the Metal-Organic Framework Compound UiO-66. *J. Mater. Chem.* **2010**, *20* (44), 9848−9851.
(39) Chu, S.; Wang, Y.; Guo, Y.; Feng, J.; Wang, C.; Luo, W.; Fan, X.; Zou, Z. Band Structure Engineering of Carbon Nitride: In Search of a Polymer Photocatalyst with High Photooxidation Property. *ACS Catal.* **2013**, *3* (5), 912−919.
(40) Liu, C.; Han, Z.; Feng, Y.; Dai, H.; Zhao, Y.; Han, N.; Zhang, Q.; Zou, Z. Ultrathin Z-scheme 2D/2D N-doped $HTiNbO_5$ Nanosheets/g-C_3N_4 Porous Composites for Efficient Photocatalytic Degradation and H_2 Generation under Visible Light. *J. Colloid Interface Sci.* **2021**, *583*, 58−70.
(41) Fan, G.; Zhan, J.; Luo, J.; Lin, J.; Qu, F.; Du, B.; You, Y.; Yan, Z. Fabrication of Heterostructured Ag/AgCl@g-C_3N_4@UiO-66(NH_2) Nanocomposite for Efficient Photocatalytic Inactivation of Microcystis Aeruginosa under Visible Light. *J. Hazard. Mater.* **2021**, *404*, 124062.
(42) Zhang, N.; Li, X.; Ye, H.; Chen, S.; Ju, H.; Liu, D.; Lin, Y.; Ye, W.; Wang, C.; Xu, Q.; et al. Oxide Defect Engineering Enables to Couple Solar Energy into Oxygen Activation. *J. Am. Chem. Soc.* **2016**, *138* (28), 8928−8935.
(43) Yuan, Q.; Liu, D.; Zhang, N.; Ye, W.; Ju, H.; Shi, L.; Long, R.; Zhu, J.; Xiong, Y. Noble-Metal-Free Janus-like Structures by Cation Exchange for Z-Scheme Photocatalytic Water Splitting under Broadband Light Irradiation. *Angew. Chem., Int. Ed.* **2017**, *56* (15), 4206−4210.
(44) Wei, J.; Shen, W.; Liu, Y. Facile Synthesis of $SrWO_4$@MIL-88A(Fe) Heterojunctions and Their Deep Treatment of Dye Wastewater and Municipal Landfill Leachate Using Photo-Fenton Technology. *J. Ind. Eng. Chem.* **2023**, *120*, 103−120.
(45) Yu, J.; Chen, Z.; Zeng, L.; Ma, Y.; Feng, Z.; Wu, Y.; Lin, H.; Zhao, L.; He, Y. Synthesis of Carbon-Doped $KNbO_3$ Photocatalyst with Excellent Performance for Photocatalytic Hydrogen Production. *Sol. Energy Mater. Sol. Cells* **2018**, *179*, 45−56.
(46) Butler, K. T.; Hendon, C. H.; Walsh, A. Electronic Chemical Potentials of Porous Metal−Organic Frameworks. *J. Am. Chem. Soc.* **2014**, *136* (7), 2703−2706.
(47) Chen, J.; Yang, Y.; Zhao, S.; Bi, F.; Song, L.; Liu, N.; Xu, J.; Wang, Y.; Zhang, X. Stable Black Phosphorus Encapsulation in Porous Mesh-like UiO-66 Promoted Charge Transfer for Photocatalytic Oxidation of Toluene and o-Dichlorobenzene: Performance, Degradation Pathway, and Mechanism. *ACS Catal.* **2022**, *12* (13), 8069−8081.
(48) Xiao, S.; Guan, Y.; Shang, H.; Li, H.; Tian, Z.; Liu, S.; Chen, W.; Yang, J. An S-scheme NH_2-UiO-66/SiC Photocatalyst *via* Microwave Synthesis with Improved CO_2 Reduction Activity. *J. CO_2 Util.* **2022**, *55*, 101806.
(49) Li, Q.; Zhou, Q.; Deng, H.; Li, Z.; Xue, B.; Liu, A.; Shen, B.; Hao, D.; Zhu, H.; Wang, Q. Schottky Heterojunction-based Photocatalysis-in-situ-Self-Fenton System: Removal of Tetracycline Hydrochloride and Biotoxicity Evaluation of Intermediates. *Appl. Catal., B* **2025**, *360*, 124533.
(50) Qaraah, F. A.; Mahyoub, S. A.; Hezam, A.; Qaraah, A.; Xin, F.; Xiu, G. Synergistic Effect of Hierarchical Structure and S-scheme Heterojunction over O-doped g-C_3N_4/N-Doped Nb_2O_5 for Highly Efficient Photocatalytic CO_2 Reduction. *Appl. Catal., B* **2022**, *315*, 121585.
(51) Li, S.; Wang, C.; Liu, Y.; Cai, M.; Wang, Y.; Zhang, H.; Guo, Y.; Zhao, W.; Wang, Z.; Chen, X. Photocatalytic Degradation of Tetracycline Antibiotic by a Novel $Bi_2Sn_2O_7$/Bi_2MoO_6 S-scheme Heterojunction: Performance, Mechanism Insight and Toxicity Assessment. *Chem. Eng. J.* **2022**, *429*, 132519.
(52) Xu, Q.; Zhang, L.; Cheng, B.; Fan, J.; Yu, J. S-Scheme Heterojunction Photocatalyst. *Chem.* **2020**, *6* (7), 1543−1559.
(53) Bi, F.; Zhao, Z.; Yang, Y.; Gao, W.; Liu, N.; Huang, Y.; Zhang, X. Chlorine-Coordinated Pd Single Atom Enhanced the Chlorine Resistance for Volatile Organic Compound Degradation: Mechanism Study. *Environ. Sci. Technol.* **2022**, *56* (23), 17321−17330.
(54) Liu, P.; Huang, Z.; Gao, X.; Hong, X.; Zhu, J.; Wang, G.; Wu, Y.; Zeng, J.; Zheng, X. Synergy between Palladium Single Atoms and Nanoparticles *via* Hydrogen Spillover for Enhancing CO_2 Photoreduction to CH_4. *Adv. Mater.* **2022**, *34* (16), 2200057.
(55) Kasimayan, U.; Nadarajan, A.; Singaravelu, C. M.; Pan, G.-T.; Kandasamy, J.; Yang, T. C. K.; Lin, J.-H. In-situ DRIFT Investigation of Photocatalytic Reduction and Oxidation Properties of SiO_2@α-Fe_2O_3 Core-Shell Decorated RGO Nanocomposite. *Sci. Rep.* **2020**, *10* (1), 2128.
(56) Liu, Y.; Chen, S.; Quan, X.; Yu, H. Efficient Electrochemical Reduction of Carbon Dioxide to Acetate on Nitrogen-Doped Nanodiamond. *J. Am. Chem. Soc.* **2015**, *137* (36), 11631−11636.
(57) Di, T.; Zhu, B.; Cheng, B.; Yu, J.; Xu, J. A Direct Z-scheme g-C_3N_4/SnS_2 Photocatalyst with Superior Visible-Light CO_2 Reduction Performance. *J. Catal.* **2017**, *352*, 532−541.
(58) Jiao, X.; Li, X.; Jin, X.; Sun, Y.; Xu, J.; Liang, L.; Ju, H.; Zhu, J.; Pan, Y.; Yan, W.; Lin, Y.; Xie, Y. Partially Oxidized SnS_2 Atomic Layers Achieving Efficient Visible-Light-Driven CO_2 Reduction. *J. Am. Chem. Soc.* **2017**, *139* (49), 18044−18051.
(59) Bi, F.; Wei, J.; Gao, B.; Liu, N.; Xu, J.; Liu, B.; Huang, Y.; Zhang, X. New Insight into the Antagonism Mechanism between Binary VOCs during Their Degradation over Pd/ZrO_2 Catalysts. *ACS ES&T Eng.* **2024**, *4* (6), 1346−1355.

https://doi.org/10.1021/jacsau.4c00998
JACS Au 2025, 5, 1184−1195

(60) Liu, Z.; Chen, Z.; Li, M.; Li, J.; Zhuang, W.; Yang, X.; Wu, S.; Zhang, J. Construction of Single Ni Atom-Immobilized ZIF-8 with Ordered Hierarchical Pore Structures for Selective CO_2 Photoreduction. *ACS Catal.* **2023**, *13* (10), 6630−6640.

https://doi.org/10.1021/jacsau.4c00998
JACS Au 2025, 5, 1184−1195